NIR-light-controlled G-quadruplex hydrogel for synergistically enhancing photodynamic therapy via sustained delivery of metformin and catalase-like activity in breast cancer

Yanting Sun [a],[1], Kang Fang [a],[1], Xiaochun Hu [a], Jingxian Yang [a], Zhengyang Jiang [a], Lei Feng [a], Ruihao Li [a], Yiming Rao [a], Shuo Shi [a],[*], Chunyan Dong [a],[**]

[a] *Department of Oncology, East Hospital Affiliated to Tongji University, School of Medicine, Shanghai Key Laboratory of Chemical Assessment and Sustainability, School of Chemical Science and Engineering, Tongji University, Shanghai 200120, PR China*

ARTICLE INFO

ABSTRACT

Severely hypoxic condition of tumour represents a notable obstacle against the efficiency of photodynamic therapy (PDT). While mitochondria targeted therapy by metformin has been considered as a promising strategy for reducing oxygen consumption in tumours, its low treatment sensitivity, short half-life and narrow absorption window in vivo remain the intractable challenges. In this report, 5′-guanosine monophosphate (5′GMP), indocyanine green (ICG), hemin and metformin, were combined to construct a smart G-quadruplex (G4) hydrogel named HMI@GEL for breast cancer (BC) treatment. Benefiting from the photothermal (PTT) effect of ICG, HMI@GEL exhibited excellent characteristics of NIR-light-triggered and persistent drug delivery to maintain high intratumoral concentration of metformin. Furthermore, drug loading concentration of metformin reached an amazing 300 mg mL^{-1} in HMI@GEL. To our knowledge, it might be the highest loading efficiency in the reported literatures. With the combination of catalase-mimicking Hemin@mil88, metformin could inhibit tumour mitochondrial respiratory significantly, which sequentially permitted in situ efficient oxygen generation. Remarkable apoptosis and necrosis were achieved by the combination of PTT and synergistically enhanced PDT as well as the activated tumour immunotherapy. Collectively, the HMI@GEL in situ injectable platform showed a promising strategy for enhanced PDT by metformin, and opened new perspectives for treating BC versatilely.

1. Introduction

According to the cancer statistics, breast cancer (BC) has become the most common carcinoma worldwide in 2021 [1]. Many treatment options were witnessed for breast cancer, including operative removal, chemotherapy, radiotherapy, endocrine therapy, and targeted therapy recently. Despite this, BC exhibits a poor prognosis that it is still the leading cause of cancer-related death for women [1]. Therefore, it is urgently demanded to develop novel therapeutic agents and methods for improving the treatment outcome of BC.

PDT, due to its high selectivity, non-invasiveness and lethal damage of tumour cells by generating tremendous cytotoxic ROS, becomes an attractive modality for anticancer therapy [2]. In the tumour microenvironment (TME), such PDT-induced antitumour process like apoptosis

and necrosis was related to T cell-mediated immune responses through induction of immunogenic cell death (ICD) [3,4]. However, these PDT induced antitumour activities were not fatal enough, typically hypoxic environment in the tumour site presented a severe obstacle [5]. To overcome this limitation, focus has now shifted to combine multimodal therapy and introduce smart nanomaterials.

Some non-chemotherapeutic drugs received widespread interest for positioned as antitumour candidates. Accumulating evidence has confirmed that a widely prescribed oral glucose-lowering medication metformin (Met), shows effectivity in almost all types of cancer including BC, lung cancer, colorectal or colon cancer et al. [6–8]. The anti-cancer properties of Met mainly depended on its regulation of cell metabolism and immune microenvironment [9]. Met effectively targeted metabolism and primarily exerted its antitumour effects through inhibition of

mitochondrial complex I to restrict the energy flow to cancer cells and made them lack of energy. It also regulated insulin activity via the insulin/insulin-like growth factor-1 (IGF-1) pathway to reduce cellular proliferation and survival [10]. However, according to Warburg effect, tumour cells typically relied on aerobic glycolysis instead of tricarboxylic acid (TCA) cycle to generate enough energy in mitochondria [11]. This largely limited the sensitivity of Met in reducing the activity of complex I in mitochondrial electron transport chain. Fortunately, reports have shown that BTB and CNC homology 1 (BACH1), which widely expressed in breast cancer, could work as a key regulator of mitochondrial glycolysis [12,13]. Intriguingly, a readily available drug hemin could regulate the subcellular localization and DNA binding of BACH1, which provided a new insight in the use of hemin to effectively enhance the sensitivity of cancer cells to Met [14]. The dual inhibition of glycolysis and TCA could further reduce the oxygen consumption of mitochondria, effectively alleviate tumour hypoxia. Additionally, the function of hemin was confirmed as oxygenase or per-oxidase, which could improve the hypoxic situation of the TME [15]. The synergistic effect of hemin and Met provided a good idea for tumour therapy. Nevertheless, the narrow absorption window in the upper gastrointestinal tract caused Met a series of restrictions for cancer treatment. Previous studies had shown that Met distributed in multiple organs after oral administration, the poor organ targeting and high doses of Met caused various adverse effects, including hypoglycaemia, lactic acidosis, gastrointestinal upset [16]. In addition, Met has an estimated plasma half-life of 1.5–4.9 h and the plasma concentration reached a peak after 3 h, making Met easy to be eliminated in vivo [17]. To maintain viable drug levels in tumour site, Met required oral high dosing frequently. However, frequent administration was very inconvenient and usually led to either poor patient compliance or treatment failure.

A variety of vectors were developed to solve these limited issues of Met, such as liposomes [18], micelles [19] and nanobubbles [20]etc. A composite by loading Met and IR775 in a liposome was constructed to enhance the production of ROS [21]. The collaborative approach based on multiple therapeutic towards cancer therapy provided a good idea to enhance its cytotoxicity to tumour cells. However, the unsatisfactory loading efficiency of Met need further improvement, which was only $26.0\% \pm 2.8\%$. Comparing typical Met drug carriers, hydrogels have attracted a lot of attentions for their unique properties, including high drug loading dose, good biocompatibility and controllable release [22]. The water-based hydrogel with smart releasing properties exactly met the drug loading requirements of water-soluble Met. The penetration, drug dissolution, change of excipient transition phase, excipient degradation, microenvironment changes and simple diffusion of hydrogel could all influence the drug release performance [23]. Properties mentioned above held great application potential in the sustained-release drug delivery. However, current research showed that the selection of suitable hydrogels was still a challenge. A heat active hydrogel formation by mixing graphene carboxyl or oxide with Met hydrochloride was reported [24]. Remarkably, it was found that activity of Met was unaffected and the hydrogel could be photothermally activated for transdermal delivery. These studies provided important ideas for the loading and controlled release of Met, but the low drug loading rate, biased functionality and complicated preparation process largely restricted them from clinic application. Therefore, how to realize the unification of functional segments including drug synergy therapy, higher drug loading rate and artificial controlled release into one platform was more challenging. 5′GMP was found to form gels for decades [25], which were assembled by stacking of G-quartets on top of one another to form extended spirals [26]. G-quadruplex hydrogels had become a new generation of smart responsive materials due to their fantastic properties, such as programmability [27], excellent injectability [28], high transparency, and rapid self-healing ability [29]. A photoactivatable dopamine-conjugated platinum complex was incorporated into G-quadruplex hydrogels via borate ester linkages, which set a good example of responsive release based on G-quadruplex hydrogels [30]. However,

there was no work about sustained or light-controlled release of Met being reported based on G-quadruplex hydrogels. The integrated advantages of hydrogels and nanoparticles launched nanoparticle–hydrogel superstructures into limelight for recent decades [31]. Benefiting from the large surface to allow the entrapping/immobilization of hemin and avoid aggregation, as well as the porous structure to facilitate the loading large amount of drugs [15], mil88 was introduced into HMI@GEL to strengthen therapeutic effect. Meanwhile, the hydrophobicity of the mil88 structure contributes to the adsorption of hemin, resulting in the enhanced catalytic properties of the nanocomposite. Furthermore, the metal ion center and organic ligand could attract more H_2O_2 to improve the catalytic activity [32]. On-site generation of O_2 is an effective mean for modulation of tumour hypoxia [33]. Exogenous catalase could be employed to alleviate hypoxia by generating O_2 from the endogenous H_2O_2 [34]. However, the property of degrading easily limits its applications [33]. The introduce of nanozymes (e.g., MnO_2 nanoparticles [35], Pt nanoparticles [36], Au nanoclusters [37]) is another way of generating O_2 [38]. However, it's not conducive to clinical application due to its poor biocompatibility, biological toxicity and high price. Fortunately, hemin has been famous for improving tumour hypoxia and enhancing the efficiency of type II PDT by virtue of its excellent catalytic functions, thermal stability, bio-affinity and cost-effectiveness [15]. For example, hemin with peroxidase-mimic catalytic activity was integrated into a radiosensitizer Hemin@Gd^{3+}/5′-GMP NCPs, which enhanced peroxidase-like properties of hemin to deplete GSH [39]. These indicated that hemin has a great potential as a peroxide-like nanozyme. Still, nanoparticle–hydrogel superstructures integrated hemin nanoparticles into G-quadruplex hydrogel has not been reported yet. Our research group was dedicated to realize controlled release of drugs and synergy of chemotherapy/phototherapy by constructing antitumour drug delivery system [40–43]. ICG was the fluorophore with high biosafety approved by the Food and Drug Administration (FDA). Beside imaging, it has attracted considerable attention because of its PDT [44]/PTT efficiency [45]. In previous work, we constructed a novel PCN–CuS-FA-ICG-based nanoplatform for dual-modal imaging-guided synergistic PDT and PTT. It was promising to achieve controlled release of Met and tumour treatment via ICG [46]. To overcome the low efficiency of PDT, we further designed a smart pH/ROS-response nanoplatform Fe^{2+}@UCM-BBD integrated chemo-dynamic therapy (CDT) and PDT to produce more ROS, with loading DOX to promote more H_2O_2 for CDT [47]. This study provided a good idea for improving ICG-mediated photodynamic therapy [47]. Meanwhile, a multifunctional nanoplatform for synergistic PDT, PTT and docetaxel-enhanced immunotherapy was successfully developed toward triple negative breast cancers [40]. The work described above about integration of phototherapy and controlled drug release provided an important basis for our research.

In this work, we constructed an in-situ injectable and NIR-light-triggered release hydrogel cross-linked by 5′GMP to realize local delivery of Met hydrochloride, which achieved light-controlled burst release and high load amount of Met in tumour site. Effective suppression of BACH1 regulated by hemin significantly enhanced the sensitivity of Met to mitochondrial complex I, which enormously improved the efficiency of ICG induced PDT. Further, the catalase activity of Hemin@mil88 produced more oxygen to overcome the limitation of tumour hypoxia. The dual enhanced ROS generation and PTT triggered by ICG under 808 nm laser irradiation caused direct tumour cell damage resulting in apoptosis or necrosis. On the other hand, tumour cell damage induced immune responses through high expressing calreticulin (CRT) reshaping the immune microenvironment successfully. Impressively, the novel hydrogel increased the loading efficiency of Met up-to 300 mg mL^{-1} in the state of the hydrogels, which was equivalent to 83.1% in the state of the dry material. As far as we knew, this was the highest drug load ability for delivery of Met in the reported literature. The new non-toxic smart hydrogel developed via the combination of PTT and significantly enhanced PDT effect, well addressed the limitations of Met and eventually offered great promise for multitherapeutic strategies of BC (Scheme 1).
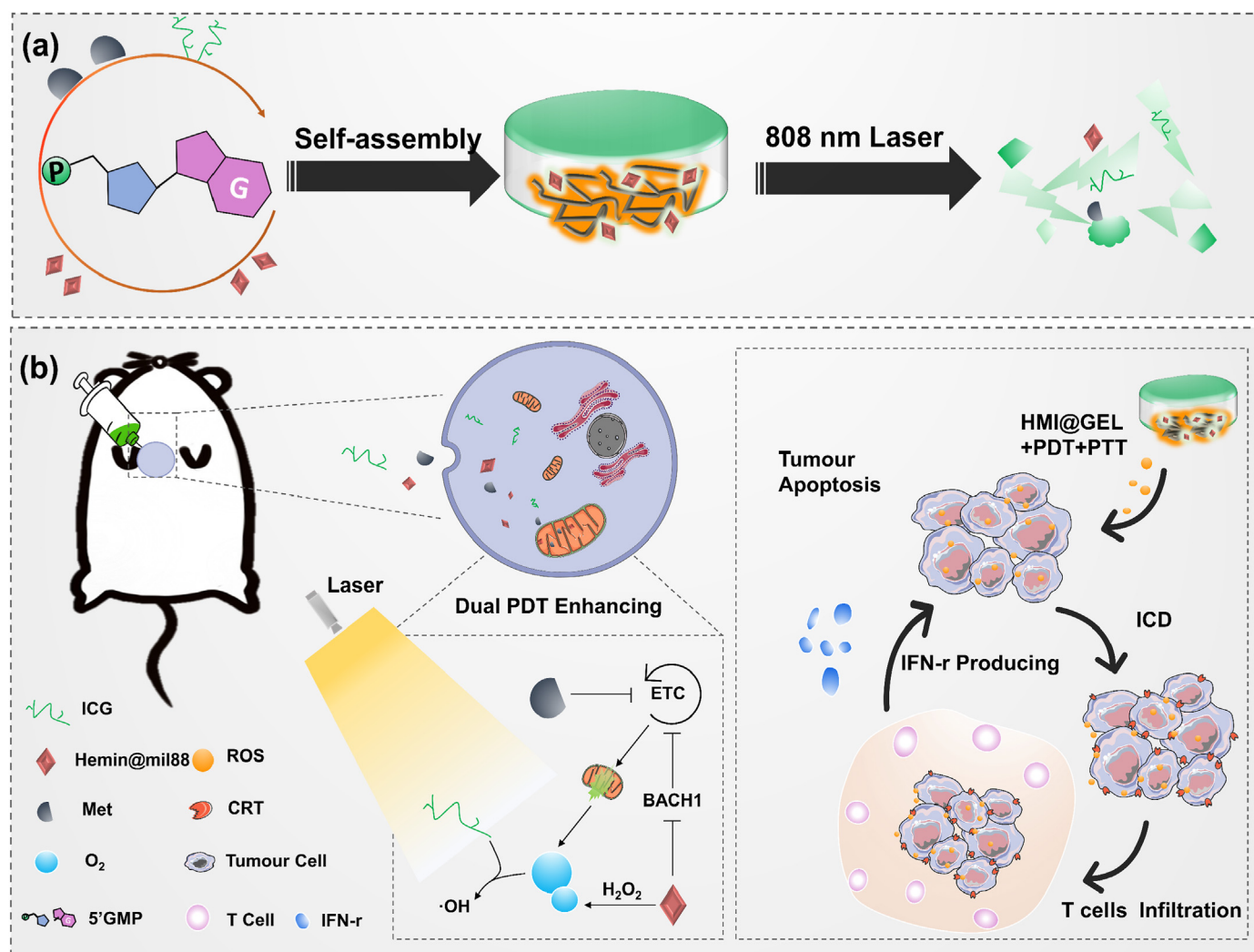
Scheme 1. Schematic illustration of HMI@GEL. (a) Rational design and synthesis of HMI@GEL hydrogel. (b) Schematic illustration of HMI@GEL hydrogel eliminates breast cancer cells in vivo under the 808 nm NIR laser irradiation.

2. Experimental methods

2.1. Synthesis and characterization of mil88, hemin@mil88 and hydrogel

Mil88 and Hemin@mil88 MOFs were synthesized referring to literature [32]. Briefly, 93.5 mg $FeCl_3 \cdot 6H_2O$ and 63 mg 2-aminoterephthalic acid were dissolved in 7.5 mL DMF. The clear mixture was then stirred at 120 °C for 4 h, and 103.58 mg acetic acid was added to the reaction solution after reacting for 15 min. After completion of the reaction, the reaction mixture was cooled to room temperature. Then the precipitate was obtained by centrifugation and repeatedly washed with DMF, ethanol and deionized water, and finally stored in deionized water for later use. Hemin@mil88 MOFs were prepared with a similar way, except that 113 mg hemin was added in the first step. 5′GMP (60 mg) and Met (300 mg) were dissolved in PBS buffer. Then 120 μL of 1 mg mL^{-1} ICG dissolved in PBS buffer and Hemin@mil88 were added. The mixture was acidified with dilute acetic acid until the pH was close to 3–4. Subsequently, the solution was made up to 1 mL with PBS buffer. Finally, HMI@GEL could be prepared by heating-cooling process with three cycles. G4 hydrogel and Met@GEL were prepared by adding 5′GMP alone or both 5′GMP and Met in a similar way. The microstructures of products were observed by scanning electron microscopy (SEM) with an accelerating voltage of 5 kV (JEM-2100, JEOL, Japan). Particle size and polydispersity index (PDI) were characterized using dynamic light scattering (DLS) (Malvern, Britain). X-ray diffraction (XRD) was determined by a D8 advance (Bruker, Germany). Mars40 rheometer (Thermo Fisher Scientific, America) was used to measure the dynamic rheological behaviour of hydrogel.

2.2. Material property characterization

The determination of the minimum gelator concentration (MGC) and stability is beneficial to clarify application, 5′GMP was dissolved in PBS buffer (1 mL) by heating, and dilute acetic acid was added to the hot solution until the expected acidity value was reached. Then the clear solution obtained was allowed to cool at specified temperature. 5′GMP of 5, 10, 15, 20, 30, 40, 50, 60, 70, 80, 100, 200 mg mL^{-1} were added to twelve vials. All the mixtures were heated over a hot plate for a few minutes and the clear solutions thus obtained at specified temperature (37, 40, 43, 46 °C). No flow of the hydrogel indicated the formation of a gel. The MGC is the minimum concentration of 5′GMP to achieve the above process. In order to evaluate the stability of the G4 hydrogel under the environment of pH 6.8 and 7.4 at 37 °C, 1 mL PBS solution was put in the freshly prepared G4 hydrogel (1 mL), and the state of the hydrogel was recorded. Determination of hemin loading is important for further biological experiment. After Hemin@mil88 was synthesized, according to the hemin standard curve, the redundant hemin collected from supernatants was determined by measuring the UV absorbance at 397 nm.

The loading efficiency (LE) of hemin were calculated by the following equations, respectively [40].

$$EE(\%) = [1 - (Concentration\,of\,loaded\,hemin)/(Concentration\,of\,devoted\,hemin)] \times 100\%$$

$$LE(\%) = [(Weight\,of\,devoted\,hemin) \times EE]/(Weight\,of\,the\,nanoparticles) \times 100\%$$

2.3. Functional measurements of materials in vitro

Catalase-like activity of Hemin@mil88 was a key factor in improving hypoxic conditions in the tumour microenvironment. 200 mM H_2O_2 was incubated in 5 mL deionized water with 120 µg mL^{-1} mil88, 120 µg mL^{-1} Hemin@mil88 or 30 µg mL^{-1} hemin (conversion based on the value of LE (%)) under 37 °C. The real-time production of oxygen was detected by an oxygen dissolving instrument. Singlet oxygen generation of ICG and HMI@Liq was beneficial to kill tumour cells. $^1O_2$ generation under the 808 nm irradiation was detected using the chemical probe 2′,7′-dichlorofluorescin diacetate (DCFH-DA). Briefly, 20 µM of DCFH was added to a solution of materials in PBS buffer whose oxygen was removed by bubbling nitrogen gas. The group included blank, H_2O_2, ICG + H_2O_2, Hemin@mil88 + ICG + H_2O_2 and HMI@Liq. Exposing for 3 min under 808 nm laser, the absorbance of DCFH at 525 nm was recorded every 30 s under excitation at 488 nm. Photothermal effect of MI@GEL and HMI@GEL was the basis of controlled-release and PTT. The photothermal effect induced by the MI@GEL was studied by irradiating gradient concentrations (60, 80, 100, 120 and 140 µg mL^{-1}) of ICG with 808 nm NIR laser at various power density (0.33, 1.5, 2.75, 4.17 W cm^{-2}) for 6 min. The temperature of MI@GEL was measured by LTX3-P Infrared Imaging (Dali Technology, Zhejiang, China). The photothermal effect of HMI@GEL were investigated by the similar method. To evaluate the photothermal stability of HMI@GEL, photothermal cycling (three cycles of laser off/on) test was carried out. In each cycle, HMI@GEL with 120 µg mL^{-1} ICG was irradiated using an 808 nm laser for 2 min, followed by naturally cooling down for 2 min without laser irradiation. Light-controlled release behaviours of Met from HMI@GEL in vitro were determined as following procedure. 808 nm NIR light was employed to investigate the photothermal effect of HMI@GEL on the release rate of Met. The concentration of released Met in the PBS solution (pH 6.8) was monitored with 30 s intervals at 231 nm wavelength by a UV/Vis spectrometer. HMI@GEL was incubated for 2 min with 5 mL PBS (pH 6.8) under dark ("OFF"), followed by another 2 min exposing time under 808 nm NIR light at 1.5 W cm^{-2}. The release rates (k_{ON} and k_{OFF}, mg mL^{-1} min^{-1}) were calculated from the concentration–time slope with and without irradiation, respectively. According to the Met standard curve, the content of Met from supernatants was determined by measuring the UV absorbance at 231 nm under Hitachi U-2900 Spectrophotometer. The degradation of HMI@GEL was evaluated by the residual rate (%). 300 µL hydrogel as Fig. S1 depicted made by 5′GMP (40, 60, 80 mg mL^{-1}) at different pH (2–3, 3–4, 5–6) were immersed in 5 mL PBS buffer at 37 °C, and hydrogel was weighted with an interval of 12 h. The degradation residue rates were calculated as the following equation (where W_t was the weight of the degraded hydrogels at various time intervals and W_0 was the weight of the initial hydrogels):

$$Degradation\,residue\,rates(\%) = (W_t / W_0) \times 100\%$$

2.4. Synergic therapeutic efficacy in vitro

Mouse mammary tumour cell 67NR were cultured in 96-well plates at a density of 1×10^4 cells/well for 24 h. Then, the culture medium of each well was replaced with another 100 µL fresh medium with different treatment (PBS, Hemin@mil88, Met, ICG + Laser, HMI@GEL, HMI@GEL + Laser) and different concentrations (5, 10, 20, 40 and 80 µg mL^{-1}), and the cells were incubated for another 24 h. The cells treated with laser were irradiated with 808 nm laser for 4 h after treatment (1.8 W cm^{-2}). At the indicated time points, the cells were incubated with CCK-8 reagent (KeyGEN, China) for 2 h at 37 °C. The BACH1 (1:500) expression of different groups was detected by Western blot. Cells were cultured in glass-bottomed dishes of 1.5×10^5 cells/dish. A reactive oxygen species assay kit (Beyotime, Shanghai) based on fluorescent probe DCFH-DA was utilized to evaluate the intracellular ROS production. Green fluorescence from DCFH-DA was excited at 488 nm wavelengths. Cells in 6-well plate were treated at an equivalent HMI@GEL concentration of 30 µg mL^{-1} for 24 h respectively. Then cells were collected, washed with cold PBS twice and fixed in cold 70% ethanol overnight. Flow cytometric analysis of apoptosis was tested using Apoptosis Analysis Kit (KeyGen, China). For CRT detection, the collected cells were incubated with anti-CRT antibodies (1:100, Abcam) for 1 h at 4 °C. Blocking of the samples was performed using blocking solution (5% donkey serum, Jackson) for 30 min. Secondary antibodies coupled to Cy3 (Beyotime, Shanghai) were dried for fluorescence observation.

2.5. Photothermal performance and biodistribution of HMI@GEL in vivo

All animal procedures conformed to the Guide for the Care and Use of Laboratory Animals of Tongji University and the ethical approval number was TJBB00721108. The female balb/c mice bearing 67NR tumours were randomly assigned to two groups, and treated with 20 µg HMI@GEL hydrogel and PBS in site for observation. The thermal images of mice were obtained by the LTX3-P infrared Imaging (DALI TECHNOLOGY, China) measured at intervals. Mice injected with HMI@Liq, HMI@GEL, and HMI@GEL + Laser were observed by BLT AniView 100 in vivo imaging system at different time points during 0–72 h. The laser treatment was irradiated with 808 nm laser after injection 0 h. Finally, the tumours and main organs of all mice were harvested for further observation in vitro.

2.6. Antitumour studies and histological analysis in vivo

67NR tumour bearing mice were divided into 7 groups randomly for the tumour inhibition experiment (n = 5). Mice were treated in site for different groups (PBS, Hemin@mil88, Met, ICG + Laser, HMI@GEL, HMI@Liq + Laser, HMI@GEL + Laser, 1 mg kG^{-1}) when the tumours reached an approximate size of 150–200 mm^3 in volume. The treatment was repeated every 3 days for a total of 5 times. The tumours were exposed to the laser irradiation (808 nm) after injection immediately. Tumour size and weight were measured at the onset of each experiment. On the 15th day, all mice were sacrificed and the tumours were excised and weighed. At the same time, the main organs (heart, liver, spleen, lung, and kidney) were obtained and stained by H&E. All tumours in every group were sliced and stained with H&E, TUNEL, ROS staining, immunofluorescence (IF) and immunohistochemistry (IHC) staining for histological analysis. Blood samples were collected by removing the eyes for testing blood routine, biochemical markers, and IFN-γ test.

2.7. Statistical analysis

All the data was performed using GraphPad Prism 8.0. The difference level between two groups was considered significance at * $p < 0.05$, **$p < 0.01$, and ***$p < 0.005$.

3. Results and discussion

3.1. Fabrication and characterization of HMI@GEL

The prepared process of the HMI@GEL platform was shown in Fig. 1a. Hemin@mil88 nanoparticles were obtained by a one-pot method based on the reaction of ferric chloride containing hemin and 2-aminotereph-thalic acid in N, N-Dimethylformamide (DMF). Hemin@mil88 showed a nearly spherical shape (Fig. 1c) with an average hydrodynamic
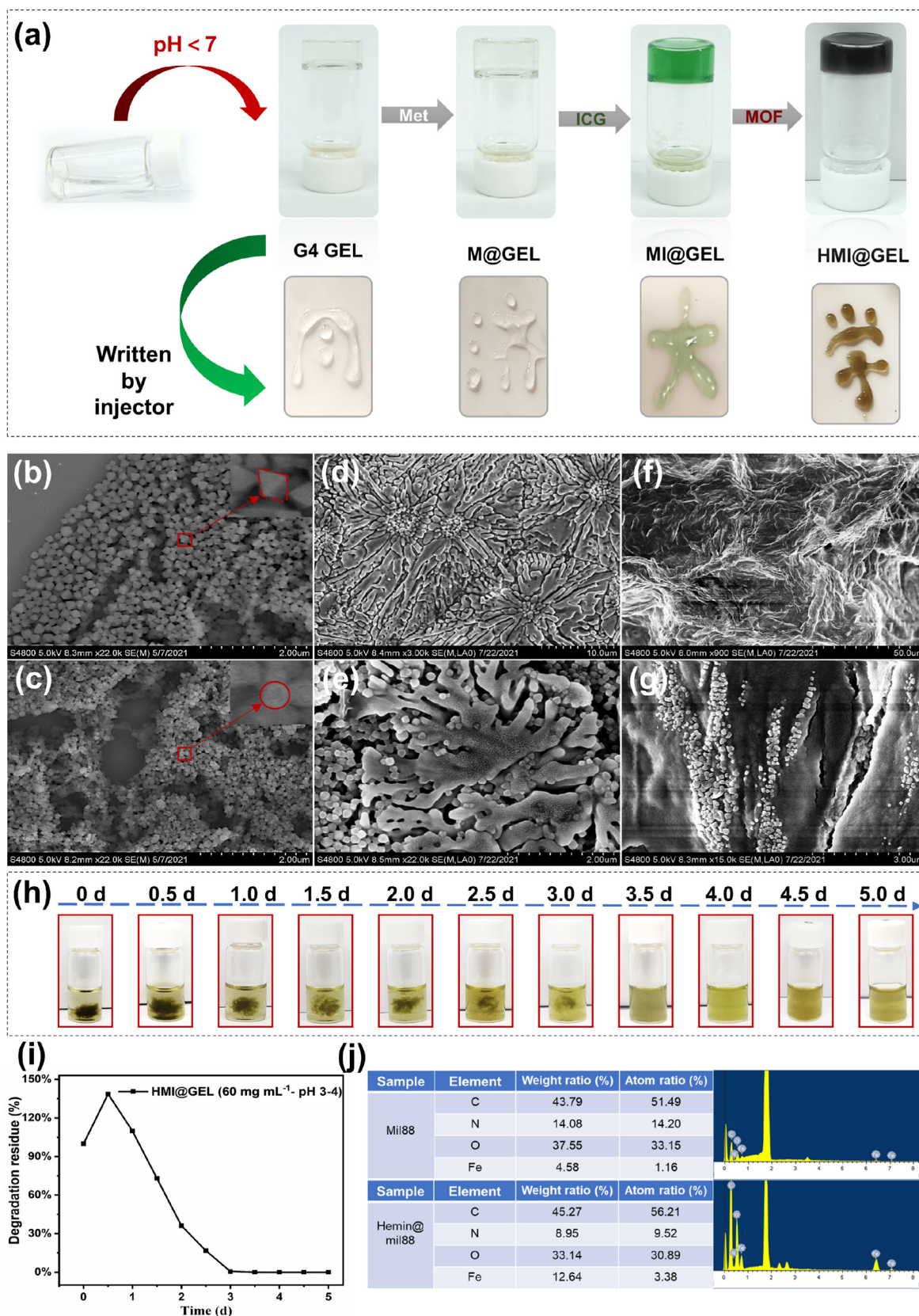
Fig. 1. (a) Photographs of the gel's preparation and writing by injection. (b–g) Representative SEM images of different groups. (b) Mil88, (c) Hemin@mil88, (d) G4 GEL with 30 mg mL^{-1} 5′GMP. (e) G4 GEL loading Hemin@mil88 with 30 mg mL^{-1} 5′GMP. (f) MI@GEL with 60 mg mL^{-1} 5′GMP. (g) HMI@GEL loading Hemin@mil88 with 60 mg mL^{-1} 5′GMP. (h) Degradation image of 300 μL HMI@GEL in 5 mL PBS at pH 6.8 over 5 days. (i) Degradation residue rate of HMI@GEL in 5 days. (j) Energy Dispersive Spectrometer (EDS) and corresponding element analysis of mil88 and Hemin@mil88.

diameter size of 204.47 nm (Fig. S1b), which was similar with mil88 (Fig. 2i, S2a), and the colour of Hemin@mil88 turned to be darker brown, indicating that hemin was successfully loaded into mil88. Compared with Hemin@mil88, mil88 MOFs showed regular octahedral shape, which demonstrated that the encapsulation of hemin in mil88 MOFs could influence the initial morphology. Meanwhile, the PDI increased from 0.25% to 16.31% (Fig. S2). SEM images and DLS results showed that the nanoparticles presented uniform morphologies. Compared with mil88, XRD patterns of Hemin@mil88 revealed similar characteristic diffraction peaks (Fig. S3), which indicated that the loaded hemin didn't change the crystallinity of mil88. According to the standard curve of hemin (Fig. S4), the UV–vis absorption spectra exhibited a characteristic peak of hemin at 397 nm, and the loading capacity of hemin was calculated about 25.15% wt.% (Fig. 2a). To further confirm the successful synthesis of Hemin@mil88 composites, energy dispersive spectroscopy (EDS) was used for elemental analysis. Compared with mil88, the weight and atomic percentage of iron element increased from 4.58% to 1.16% up to 12.64% and 3.38% (Fig. 1j). The above results were consistent with the previous report [32], which further

demonstrated the successful preparation of Hemin@mil88. HMI@GEL were prepared by a cocktail method based on the reaction of Hemin@mil88, Met, 5′GMP and ICG in acidic PBS buffer. Referring to the changes of minimum gelation concentration (Table S1), the stability (Table S2, Table S3) of the hydrogel increased along with the increased acidity and concentration of 5′GMP. G-quadruplex hydrogel exhibited a process of softening-collapsing-gelling in a pH 6.8 environment, but it was less obvious in the pH 7.4 environment. The physical property was beneficial to the construction of vectors for in situ induced robust hydrogel [48]. The above optimal gelation experiments indicated that hydrogel formed in PBS buffer at pH 6.8 showed relatively stable gelation and collapse properties, when the concentration of 5′GMP was adjusted to 60 mg mL^{-1}. Therefore, the hydrogel formed under this condition could be used as a drug-transport ship targeted the acidic tumour microenvironment. It was remarkable that the loaded amount of Met reached an amazing 300 mg mL^{-1} in a gel-like state, which was equivalent to 83.1% in a freeze-dried state. To the best of our knowledge, it might be the highest loading efficiency in the reported literatures. Light-to-heat conversion effect of hydrogel was positively correlated with
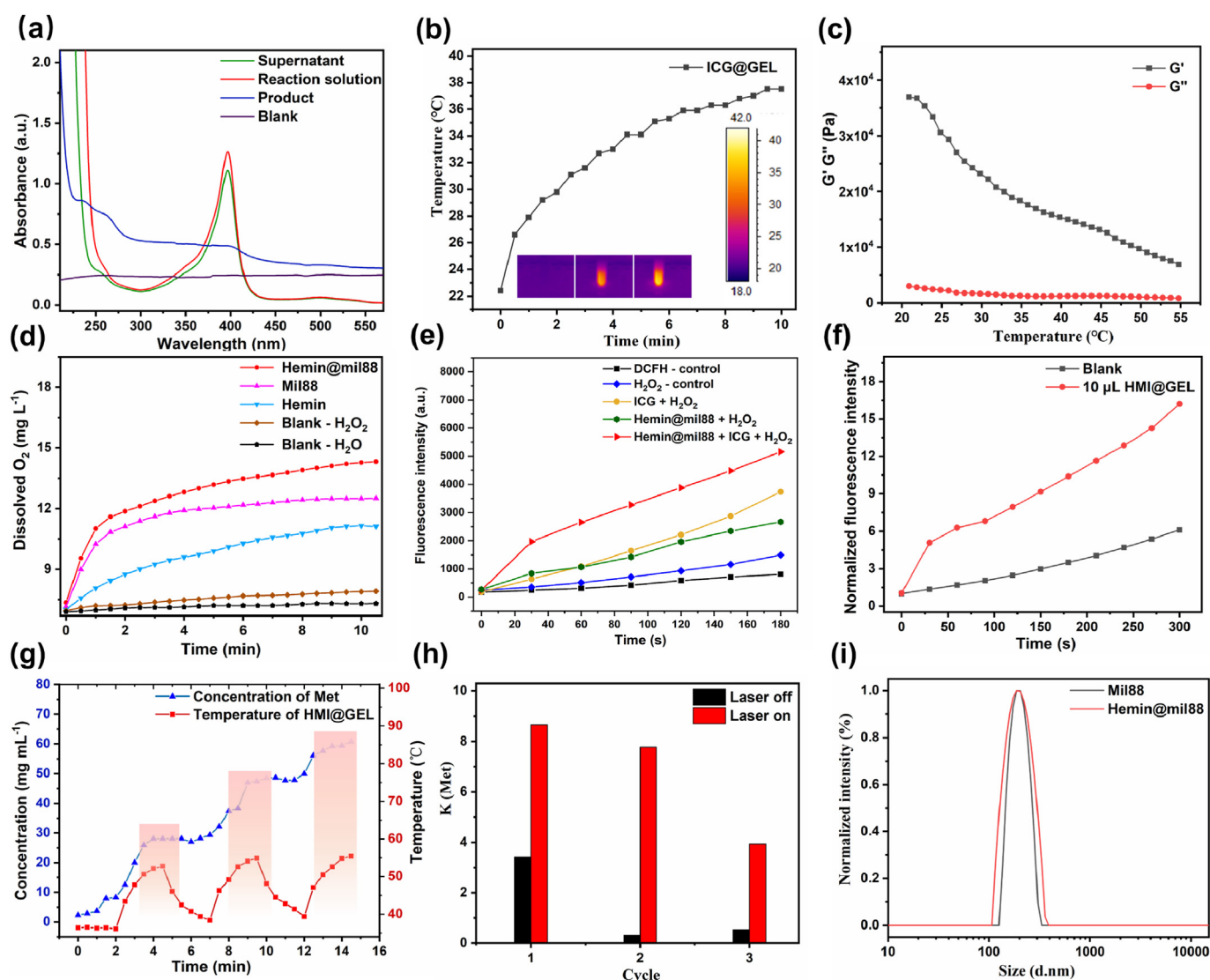

Fig. 2. Key functional properties. (a) UV–visible absorption spectra of different nanoparticles and free hemin. (b) Temperature changes of ICG@GEL at 120 mg mL^{-1} ICG under 1.5 W cm^{-2} irradiation. (c) The G′ and G″ changes of HMI@GEL as the temperature slowly increases. (d) Catalase-like activity of Hemin@mil88. (e) $^1O_2$ generation of ICG under the influence of Hemin@mil88. (f) $^1O_2$ generation of 10 μL HMI@GEL under the influence of Hemin@mil88. (g) Photo-controlled temperature increase and release of Met from HMI@GEL. (h) Release rate of Met with and without laser exposure. That k_{ON} was much higher than k_{OFF}, indicating that HMI@GEL could work as an effective optical switch of Met release. (i) DLS of mil88 and Hemin@mil88.

the increase of ICG concentration and radiation power (Fig. S5). Hydrogel induced a temperature increase of 11.7 °C in 5 min with 120 μg mL^{-1} ICG under 1.5 W cm^{-2} laser radiation power, which could fully meet the requirements of photothermal controlled release of Met (Fig. 2b). Increasing the concentration of 5′GMP from 30 mg mL^{-1} to 60 mg mL^{-1}, the morphologies of hydrogel showed that radial branches merged with each other to form a planar microscopic morphology (Fig. 1d and f), and Hemin@mil88 nanoparticles still kept adhering to the surface of the hydrogel (Fig. 1e and g). The above comprehensive morphological characterization confirmed the successful synthesis of HMI@GEL.

3.2. Functional characterization of HMI@GEL

Four functional characteristics of HMI@GEL were evaluated as follows. Degradability of hydrogel played an important role in drug release process. Compared with the initial state of HMI@GEL, a gradual dissociation process from inside to outside was observed, including swell by absorbing water, reducing adhesion, transparent of edge and collapse sections (Fig. 1h). As demonstrated in Fig. S6, the dissociation process of hydrogel was obviously influenced by pH values. Compared with hydrogel under weak alkaline conditions (pH: 7.4), hydrogel under weak acid conditions (pH: 6.8) exhibited slightly stronger degradation resistance, and this performance was more obviously at pH 5.0, which indicated that the hydrogel could exhibit stronger retention effect in slightly acidic tumour environment. As demonstrated in Fig. S7, resistance to degradation of hydrogel increased along with the increased acidity and concentration of 5′GMP. Referring to the complete degradation time of 3 days, hydrogel prepared with 60 mg mL^{-1} 5′GMP and pH 3–4 was selected to support further work. Rheological behaviour of HMI@GEL (Fig. S8) exhibited that HMI@GEL was a kind of non-Newtonian and pseudoplastic fluid. As the temperature rose, the storage modulus and viscosity of the gel decreased rapidly (Fig. 2c). In addition, viscoelastic ratio increases rapidly over 35 °C (Fig. S8c), which indicated temperature could change the viscosity of HMI@GEL significantly. The above results supported the controlled release of Met. Photodynamic effect of HMI@-GEL was directly related to the improvement of hypoxic environment. Amplification catalase-like activity was evaluated using the amount of dissolved oxygen as an indicator. As shown in Fig. 2d, the catalytic ability of hemin for hydrogen peroxide appreciably increased by 31.19% under the catalysis of mil88, which contributed to enhancing the photodynamic effect of ICG (Fig. 2e). Impressively, only 10 μL HMI@GEL generated a large amount of reactive oxygen species (Fig. 2f), which could effectively kill tumour cells. As the most important part, according to the standard curve of Met (Fig. S9), the light-controlled release capability of Met was assessed under an 808 nm near infrared laser irradiation with a power density of 1.5 W cm^{-2} (Fig. 2g). Compared with slower release of Met without irradiation, the concentration of Met increased dramatically under irradiation. Release rates (k_{ON} and k_{OFF}, mg mL^{-1} min^{-1}) were measured by the slope of the drug release profile in the presence or absence of light exposure (Fig. 2h), which showed.

3.3. HMI@GEL hydrogel synergistically sensitized photodynamic and apoptosis in vitro

Tumour hypoxia is a significant obstacle to PDT, inspired by excellent catalase-like activity of Hemin@mil88 in the above experiments, the high expressed hypoxia-inducible factor-1α (HIF-1α) activated in cancer was utilized to detect the hypoxic level. As shown in Figs. S10a and b, after treating with Hemin@mil88, the expression of HIF-1α was decreased in 67NR cell. In addition, the treatment of Met also led to a reduction of HIF-1α, which might alleviate hypoxic situation to some extent. In particular, the synergistic function of hydrogel HMI@GEL showed the strongest inhibition of HIF-1α. Then, the intracellular PDT efficiency was investigated in vitro. DCFH-DA ROS fluorescent probe was utilized for detecting intracellular ROS generation. Nearly no

fluorescence was observed inside the cells by confocal laser scanning microscopy (CLSM) after treating with PBS. Faint fluorescence signal was presented in Hemin@mil88 and Met group. Expectedly, since the combined treatment of Met and Hemin@mil88 further alleviated tumour hypoxia, the fluorescence signal was significantly enhanced after HMI@GEL treatment. Compared to mono-ICG group, obvious green fluorescence was observed for ICG/He/Met group after light irradiation (Fig. 3e, Fig. S11). Notably, when treated with HMI@GEL, tumour cells exhibited the strongest green fluorescence than other groups at the same concentration. Subsequently, this phenomenon was further validated by classical flow cytometry (Fig. 3e). Concurrently, the lower protein expression levels of BACH1 in both Hemin@mil88 and HMI@GEL groups compared with the control group from Western blot indicated that the HMI@GEL platform containing hemin could inhibit the expression of BACH1 effectively (Fig. 3b). Therefore, the integration of Met and Hemin@mil88 greatly reduced the limitation of PDT caused by intracellular hypoxia, and achieved the goal of producing more ROS through the dual sensitizing PDT. Based on the excellent PDT effect, the therapeutic efficacy of the hydrogel was evaluated by CCK-8 assay in vitro. As shown in Fig. 3g, there was nearly no toxic effect of crosslinker 5′GMP on cell activity. Similarly, cells in control group (PBS) were nearly totally alive and little cell death was observed by the treatment of Hemin@mil88 (Fig. 3a). Cell survival rate in HMI@GEL hydrogel group was significantly less than that of Met or ICG + Laser group only. Moreover, cells cultured with HMI@GEL hydrogel under 808 nm irradiation exhibited the strongest cytotoxicity (Fig. 3a). This suggested that HMI@GEL hydrogel present promising therapeutic benefited for breast cancer cells. To detect the apoptosis of 67NR cells after treatments, a quantification of flow cytometry analysis was performed by Annexin V-PI staining. In Fig. 3c, almost all cells in control group (PBS) were in the lower left quadrant (Q4, live cells), cells from other groups migrated to other quadrants, which meant the treated cells endured different degrees of apoptosis. As for the treatment with HMI@GEL under 808 nm laser, the apoptotic levels of cells were significantly increased compared with that in the HMI@GEL or ICG + Laser group, indicating that the synergistic treatment more potently enhanced the late apoptosis triggered cell death by inducing the generation of ROS (Fig. 3f).

3.4. PTT/PDT related CRT overexpression on tumour cell surface in vitro

ICD has been widely observed for PTT and PDT [49–51]. ROS generation by PDT is essential for the activation of signal pathways that govern ICD [52]. These therapies induce the expression of tumour antigens like CRT, consequently implementing tumour immunogenicity. For the evaluation of CRT expressing on the surface of tumour cells, the 67NR cells with different treatments were analysed by flow cytometry (the histograms on the right are for the quantification analysis). The low fluorescence intensity indicated that Hemin@mil88 and Met slightly induced CRT expression on the surface of tumour cells (Fig. 3d). In contrast, for the HMI@GEL group with laser, CRT expression obviously increased under the synergistic therapy along with the remarkable elevation of ROS generation. As showed in Fig. 3d, the fluorescence intensity of CRT in HMI@GEL hydrogel with 808 nm laser was more than twice that of the other treatments. These observations demonstrated that the novel hydrogel HMI@GEL-mediated dual enhanced PDT efficiently induced high expression of CRT on 67NR cell surface.

3.5. Photothermal and sustained-release performance of HMI@GEL in vivo

To detect the photothermal performance of HMI@GEL hydrogel in vivo, animal NIR images and temperature of tumour site was then evaluated respectively after intratumoural injection of HMI@GEL and PBS under irradiation. After irradiation for 5 min, the local tumour temperature of the HMI@GEL group rapidly rose up to 44.8 °C while a slight increase (2 °C) was observed in the PBS group, which revealed its good
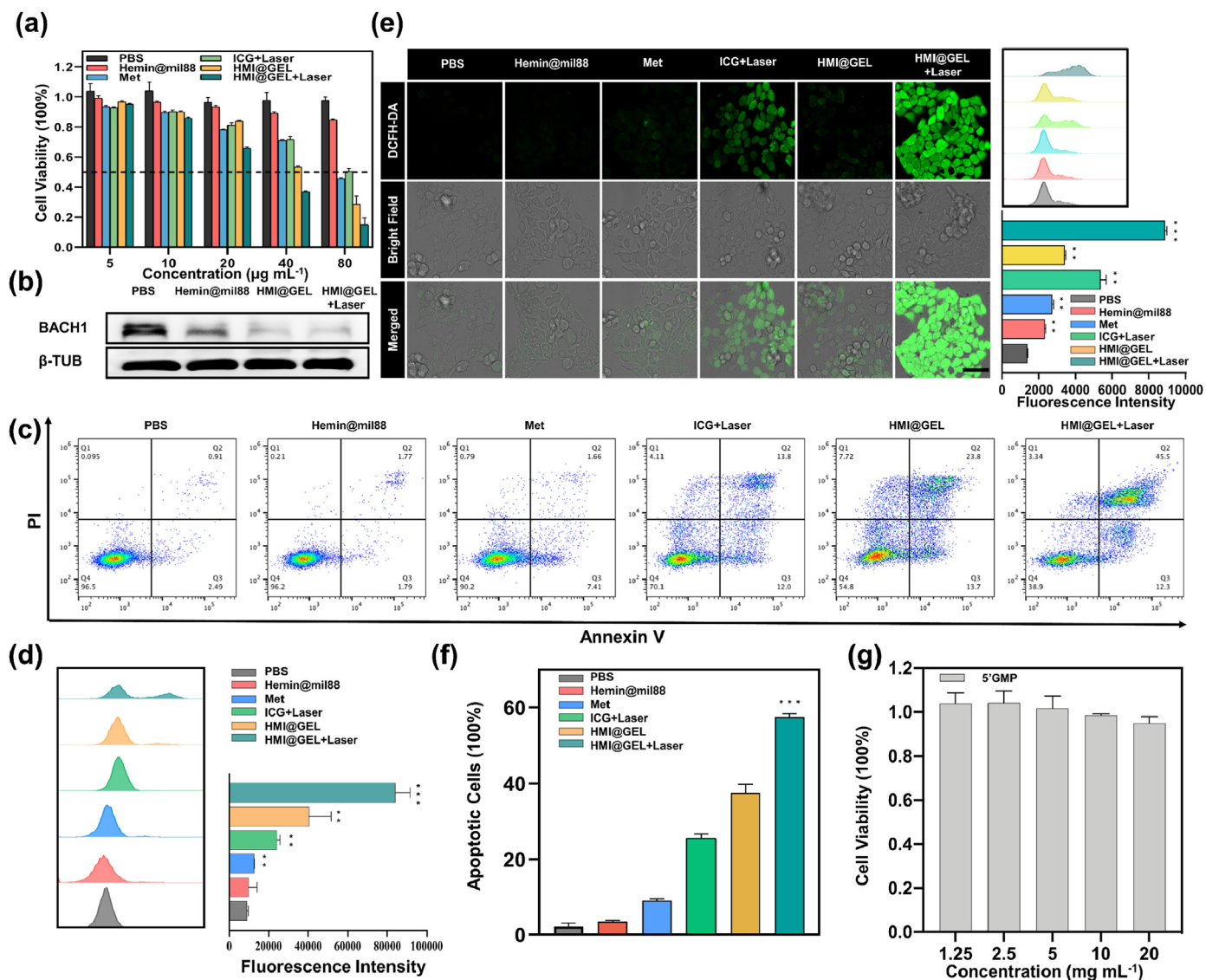
Fig. 3. In vitro synergetic photodynamic therapy of HMI@GEL. (a) Cytotoxicity of 67NR cells after different treatment for 24 h via CCK-8 assay. (b) Western blot analysis of BACH1 in PBS, Hemin@mil88, HMI@GEL and HMI@GEL + Laser treatment groups. (c) Flow cytometry analysis of apoptosis rate under different conditions. (d) Flow cytometric assay of CRT expression after 24 h. (e) CLSM images and flow cytometry analysis of intracellular ROS level incubated with different treatment. (f) Flow cytometry quantitative analysis of total apoptosis rate under different conditions. (g) Cytotoxicity of 67NR cells treated with 5′GMP for 24 h via CCK-8 assay. Scale bar = 50 μm p values: **p < 0.01, and ***p < 0.001 vs. PBS group.

photothermal therapeutic potential (Fig. 4a and b). When hydrogel was injected in tumour site, it was usually confined in a pressurized environment and constantly interacted with body fluid, which was definitely different from an in vitro setting. Therefore, live animal imaging technology was utilized to further evaluate the intratumoural retention of three treatments (HMI@Liq, HMI@GEL, HMI@GEL + Laser) on mice bearing orthotopic breast cancer tumours. The dynamic change of fluorescence at 0 h, 12 h, 24 h, 48 h, 60 h and 72 h after intratumoural injection was monitored. As presented in Fig. 4c, hydrogel samples intratumoural injection exhibited an obviously localized drug distribution around the tumour site and more sustained release over 72 h than intratumoural injection of ICG free (HMI@Liq). Moreover, although our hydrogel platform was more easily degraded under photothermal, its sustained-release effect was not affected in vivo after 5 min of irradiation. The hydrogel in two groups (with or without 808 nm laser) were both metabolized about 72 h. In addition, the primary distribution of in situ injected hydrogel HMI@GEL is at the tumour site, there is little residue of the drugs in the main organs during 72 h treatment. Then, the mice were sacrificed subsequently to isolate tumours and main organs for

metabolism observation. The drug fluorescence in tumour sites and organs were hardly visible, indicating the excellent biological safety of this novel hydrogel platform (Fig. 4c).

3.6. Tumour eradication and immune responses after in situ injecting HML@GEL via in vivo assessments

Based on the biological effects above, an in vivo antitumour experiment was carried out to validate the antitumour and immune infiltration effect of breast cancer. An orthotopic 67NR mammary tumour model was prepared and monitored ranged from 1 to 15 days (Fig. 4d). The tumour bearing mice were randomly divided into seven groups and treated as follows: control group: PBS; mono therapy groups: Hemin@mil88, Met, PDT + PTT (ICG + Laser), hydrogel only (HMI@GEL); combination therapy groups: non-gelatinous mixture of three drugs with laser irradiation (HMI@Liq + Laser), HMI@GEL with laser irradiation (HMI@GEL + Laser). Noticeably, in line with the results of the tumour volume and weight shown in Fig. 4e–g, the tumour-inhibiting efficiencies of mono therapy groups were worse than those of combination therapy groups.
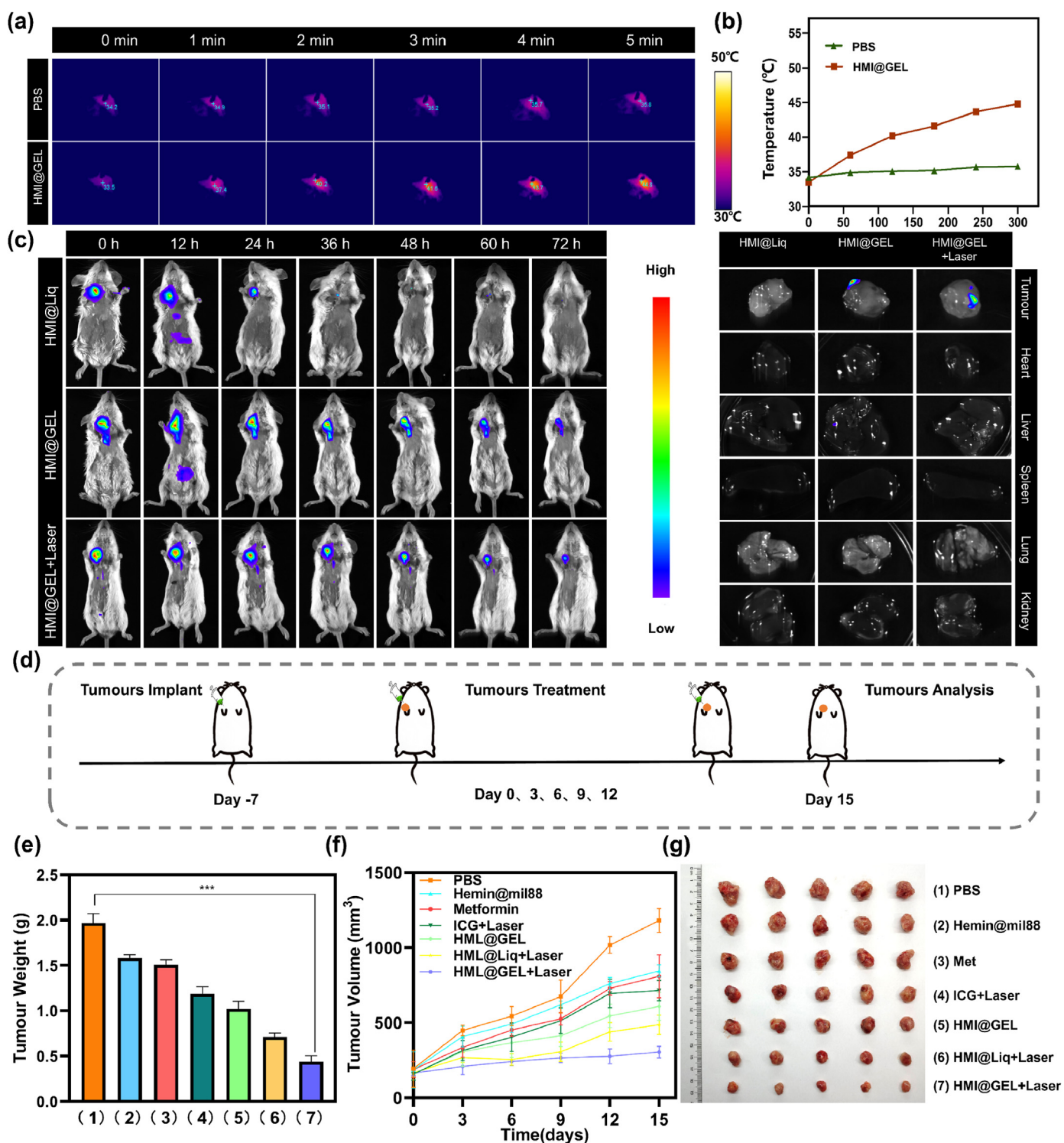
Fig. 4. (a) The in vivo photothermal images of the mice after in situ injection of PBS and HMI@GEL with 808 nm laser irradiation for 5 min. (b) Photothermal heating curves of tumour tissues as a function of irradiation time. (c) Fluorescence images of the mice and organs at 72 h post injection of HMI@Liq, HMI@GEL and HMI@GEL + Laser. (d) Schematic illustration of treatment process in mice. (e) Histogram of mean tumour weight measured on day 15. (f) Tumour volume curves. (g) Representative images of tumour in different groups obtained on day 15th. HMI@Liq: Hemin@mil88 + Met + ICG Liquid. p values: ***p < 0.001 vs. PBS group.

Compared to the Hemin@mil88, Met, and ICG + Laser groups, the hydrogel group HMI@GEL could suppress the tumour growth better, but were still comprehensively less efficient than the combination therapy groups with 808 nm laser. The expression of HIF-1α was reduced after treating with hemin@mil88 and Met, especially in HMI@GEL group, which meant the intratumoural hypoxia was efficiently ameliorated (Fig. S10c). This indicated that synergism of hemin@mil88 and Met

successfully inhibited tumour growth in vivo through enhancing PDT efficiency, which could be strongly confirmed by the ROS fluorescence staining of tumour tissues (Fig. 5a, Fig. S12). Meanwhile, the largest necrotic areas with no cell structures in HMI@GEL + Laser group than other groups were observed by H&E staining (Fig. 5a). Apoptosis was measured by TUNEL assay and Caspase-3 IHC staining, HMI@GEL + Laser group demonstrated a marked increase in TUNEL positive and
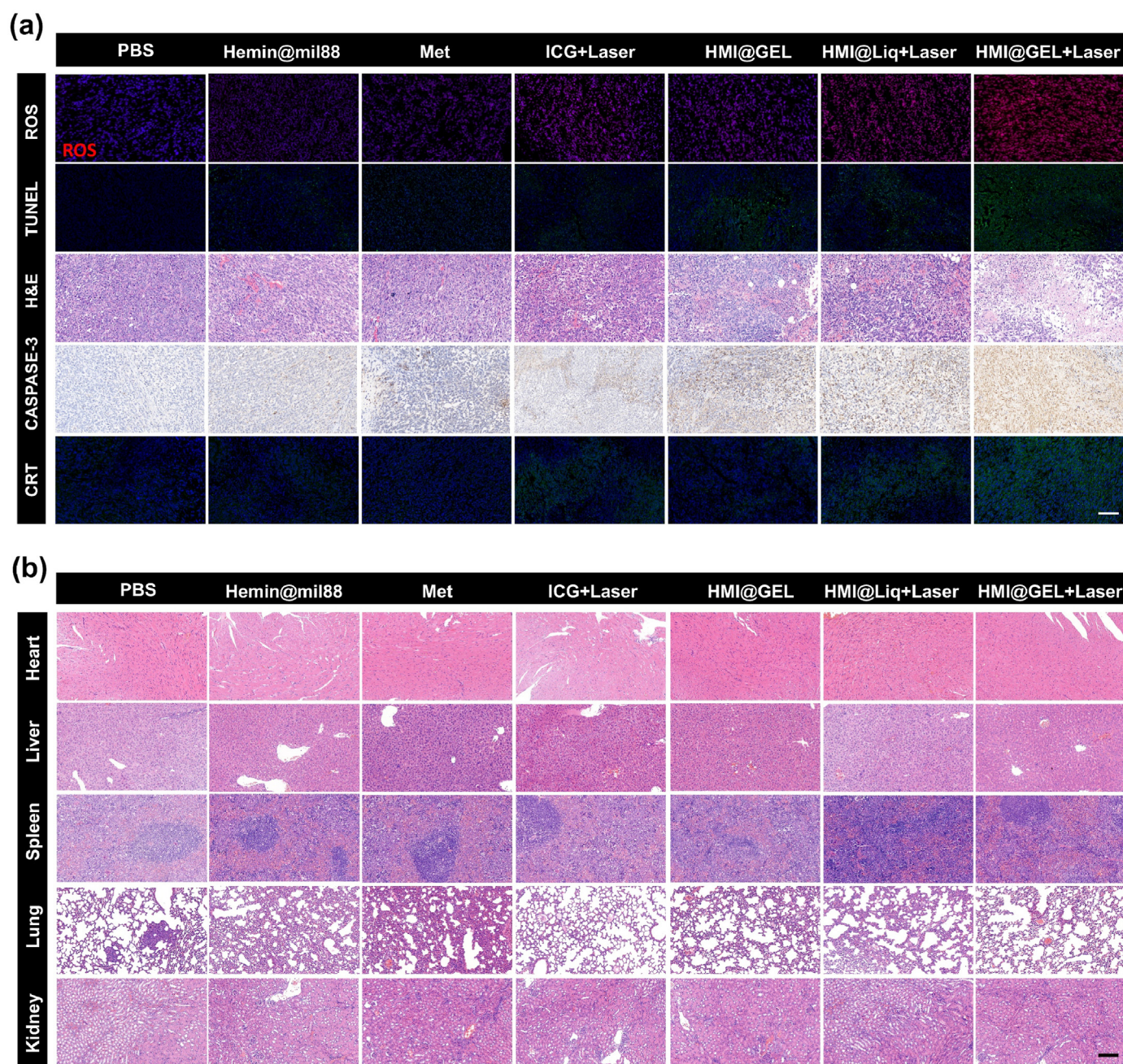
Fig. 5. H&E, TUNEL (green) staining, immunofluorescence staining of ROS (red), CRT (green) and immunohistochemical staining images of Caspase-3 of tumour sections subjected to different treatments after 15 days. (b) H&E staining of main organs (heart, liver, spleen, lung and kidney) from mice after treatment. Scale bar = 100 μm.

Caspase-3 positive cells, indicating that the cell apoptosis was considerably facilitated by HMI@GEL + Laser treatment (Fig. 5a). Further, the tumour volume of the HMI@GEL + Laser group were obviously smaller than those of HMI@Liq + Laser group, which clearly demonstrated that sustained release caused by the hydrogel platform effectively prolonged the drug metabolism and achieved the better anti-tumour efficacy in vivo.

Since the apoptosis induced by PTT and enhanced PDT elicited an immune response by inducing ICD of the tumour, the expression of CRT was evaluated for ICD study in vivo. As shown in Fig. 5a, immunofluorescence analysis revealed that CRT expression level in HMI@GEL + Laser group was significantly higher than other groups, which corresponded well with the PDT performance and apoptosis in vivo. CRT

surface expression on apoptosis tumour cells could send a "eat me" signal, attract and activate antigen presenting cells like dendritic cells (DCs) [53]. Mature DCs recruit naive $CD4^+$ and $CD8^+$ T cells, aiding in the clonal expansion of cytotoxic T lymphocytic cells (CTLs), thus leading to activation of adaptive immunity [54,55]. To better understand the existence of tumour infiltrating lymphocytes (TILs), infiltration of $CD4^+$ and $CD8^+$ T cells after different treatments were further visualized by immunofluorescence. As depicted in Fig. S13, HMI@GEL with 808 nm laser irradiation could elicit the production of $CD4^+$ and $CD8^+$ T cells well within the TME, along with enhancing secretion of cytokine interferon-gamma (IFN-γ) (Fig. S14). This further indicated that this PDT enhanced gel elicited antitumour adaptive immunity and destroy tumour cells efficiently in vivo.

3.7. Biosafety analysis in vivo

Since the anti-tumour properties of the hydrogel was proved after 15 days treatment in vivo, to further explore the biosafety and biocompatibility, organs were excised from mice and stained by

H&E. All side effects of the main organs were negligible (Fig. 5b). No serious adverse reactions were identified such as diarrhoea, vomiting, or significant body weight loss in any of the treated groups during this period (Fig. S15). Besides, blood samples of the mice were also collected for evaluating the degree of myelosuppression and the function of liver and kidney. Differences in the serum biochemical indicators including white blood cell count (WBC), hemoglobin (Hb), platelet (PLT), serum aspartate aminotransferase (AST), alanine aminotransferase (ALT), creatinine (CREA) between control and treated groups were not statistically significant (Fig. S16). Collectively, the above results confirmed that HMI@GEL platform showed almost no toxic effect on different organs and were promising for potential clinical applications.

4. Conclusions

A smart NIR light-to-heat controlled drug-release hydrogel was fabricated by 5′GMP and ICG. After loading Met and Hemin@mil88, we achieved the synergistic therapy of the drugs and light-controlled drug release synchronously. After injection, the controllable gel HMI@GEL resulted in a light-triggered Met release under 808 nm NIR laser. What worth paying attention to is the Met release rate can be tuned by external manipulation, which is beneficial to maintain an effective drug concentration in clinical application.

Due to the dual inhibition of glycolysis and TCA by the synergistic utilization of hemin and Met, the oxygen consumption of mitochondria could be reduced obviously. Moreover, Hemin@mil88 substantially created new catalase-like activity, which made the gel overcome hypoxia in tumour site and improve PDT effectively. Further, according to the high drug-loading feature of gel, ICG under 808 nm NIR laser showed great PTT efficiency and produced a large amount of ROS to promote cancer cell apoptosis simultaneously. More attractively, PTT, along with the dual enhanced PDT effect induced high expression of CRT to active adaptive immunity and then improved tumour immunotherapy successfully. Additionally, biosafety analysis presented HMI@GEL platform showed hardly toxic effect on main organs. In all, this in site injectable multifunctional hydrogel HMI@GEL offered a new therapeutic opportunity for breast cancer.

Declaration of Competing Interests.

The authors declare that they have no known competing financial interests or personal relationships that could have appeared to influence the work reported in this paper.

Credit author statement

Yanting Sun and **Kang Fang**: Conceptualization, Methodology, Formal analysis, Investigation, Data curation, Writing-original draft, Writing-review & editing, Visualization. **Xiaochun Hu** and **Jingxian Yang**: Methodology, Formal analysis, Investigation, Data curation. **Zhengyang Jiang**, **Yiming Rao** and **Ruihao Li**: Methodology, Formal analysis. **Chunyan Dong**, **Shuo Shi** and **Lei Feng**: Conceptualization, Resources, Writing-review & editing, Supervision, Project administration, Funding acquisition.

Declaration of competing interest

The authors declare that they have no known competing financial interests or personal relationships that could have appeared to influence the work reported in this paper.

Appendix A. Supplementary data

Supplementary data to this article can be found online at https://doi.org/10.1016/j.mtbio.2022.100375.

References

[1] R.L. Siegel, K.D. Miller, H.E. Fuchs, A. Jemal, Cancer statistics, 2021, CA A Cancer J. Clin. 71 (2021) 7–33.

[2] Y. Ding, R. Yang, W. Yu, C. Hu, Z. Zhang, D. Liu, Y. An, X. Wang, C. He, P. Liu, Q. Tang, D. Chen, Chitosan oligosaccharide decorated liposomes combined with TH302 for photodynamic therapy in triple negative breast cancer, J. Nanobiotechnol. 19 (2021) 147.

[3] F. Jin, D. Liu, X. Xu, J. Ji, Y. Du, Nanomaterials-based photodynamic therapy with combined treatment improves antitumor efficacy through boosting immunogenic cell death, Int. J. Nanomed. 16 (2021) 4693–4712.

[4] Z. Su, Z. Xiao, J. Huang, Y. Wang, Y. An, H. Xiao, Y. Peng, P. Pang, S. Han, K. Zhu, X. Shuai, Dual-sensitive PEG-sheddable nanodrug hierarchically incorporating PD-L1 antibody and zinc phthalocyanine for improved immuno-photodynamic therapy, Acs Appl Mater Inter 13 (2021) 12845–12856.

[5] Y. Liu, Y. Jiang, M. Zhang, Z. Tang, M. He, W. Bu, Modulating hypoxia via nanomaterials chemistry for efficient treatment of solid tumors, Acc. Chem. Res. 51 (2018) 2502–2511.

[6] L. Cheng, X. Zhang, Y.Z. Huang, Y.L. Zhu, L.Y. Xu, Z. Li, X.Y. Dai, L. Shi, X.J. Zhou, J.F. Wei, Q. Ding, Metformin exhibits antiproliferation activity in breast cancer via miR-483-3p/METTL3/m(6)A/p21 pathway, Oncogenesis 10 (2021) 7.

[7] M.N.A. Kamarudin, M.M.R. Sarker, J.R. Zhou, I. Parhar, Metformin in colorectal cancer: molecular mechanism, preclinical and clinical aspects, J. Exp. Clin. Cancer Res. 38 (2019) 491.

[8] J. Kang, S.M. Jeong, D.W. Shin, M. Cho, J.H. Cho, J. Kim, The associations of aspirin, statins, and metformin with lung cancer risk and related mortality: a time-dependent analysis of population-based nationally representative data, J. Thorac. Oncol. 16 (2021) 76–88.

[9] Z. Lv, Y. Guo, Metformin and its benefits for various diseases, Front. Endocrinol. 11 (2020) 191.

[10] A. De, G. Kuppusamy, Metformin in breast cancer: preclinical and clinical evidence, Curr. Probl. Cancer 44 (2020), 100488.

[11] O. Warburg, On the origin of cancer cells, Science 123 (1956) 309–314.

[12] X. Zhang, J. Guo, X. Wei, C. Niu, M. Jia, Q. Li, D. Meng, Bach1: function, regulation, and involvement in disease, Oxid. Med. Cell. Longev. (2018), 1347969, 2018.

[13] J. Lee, A.E. Yesilkanal, J.P. Wynne, C. Frankenberger, J. Liu, J. Yan, M. Elbaz, D.C. Rabe, F.D. Rustandy, P. Tiwari, E.A. Grossman, P.C. Hart, C. Kang, S.M. Sanderson, J. Andrade, D.K. Nomura, M.G. Bonini, J.W. Locasale, M.R. Rosner, Effective breast cancer combination therapy targeting BACH1 and mitochondrial metabolism, Nature 568 (2019) 254–258.

[14] H. Suzuki, S. Tashiro, S. Hira, J. Sun, C. Yamazaki, Y. Zenke, M. Ikeda-Saito, M. Yoshida, K. Igarashi, Heme regulates gene expression by triggering Crm1-dependent nuclear export of Bach1, EMBO J. 23 (2004) 2544–2553.

[15] A.M. Alsharabasy, A. Pandit, P. Farras, Recent advances in the design and sensing applications of hemin/coordination polymer-based nanocomposites, Adv. Mater. 33 (2021), e2003883.

[16] S. Abdelghaffar, A.M. Attia, Metformin added to insulin therapy for type 1 diabetes mellitus in adolescents, Cochrane Database Syst. Rev. 1 (2009) CD006691.

[17] C.J. Bailey, R.C. Turner, Metformin, N Engl J Med. 334 (1996) 574–579.

[18] Z. Yang, J. Wang, S. Liu, X. Li, L. Miao, B. Yang, C. Zhang, J. He, S. Ai, W. Guan, Defeating relapsed and refractory malignancies through a nano-enabled mitochondria-mediated respiratory inhibition and damage pathway, Biomaterials 229 (2020), 119580.

[19] T. Jiang, L. Chen, Y. Huang, J. Wang, M. Xu, S. Zhou, X. Gu, Y. Chen, K. Liang, Y. Pei, Q. Song, S. Liu, F. Ma, H. Lu, X. Gao, J. Chen, Metformin and docosahexaenoic acid hybrid micelles for premetastatic niche modulation and tumor metastasis suppression, Nano Lett. 19 (2019) 3548–3562.

[20] M. Zhao, X. Yang, H. Fu, C. Chen, Y. Zhang, Z. Wu, Y. Duan, Y. Sun, Immune/Hypoxic tumor microenvironment regulation-enhanced photodynamic treatment realized by pH-responsive phase transition-targeting nanobubbles, ACS Appl. Mater. Interfaces 13 (2021) 32763–32779.

[21] W. Xiong, L. Qi, N. Jiang, Q. Zhao, L. Chen, X. Jiang, Y. Li, Z. Zhou, J. Shen, Metformin liposome-mediated PD-L1 downregulation for amplifying the photodynamic immunotherapy efficacy, ACS Appl. Mater. Interfaces 13 (2021) 8026–8041.

[22] S. Correa, A.K. Grosskopf, H. Lopez Hernandez, D. Chan, A.C. Yu, L.M. Stapleton, E.A. Appel, Translational applications of hydrogels, Chem. Rev. 121 (2021) 11385–11457.

[23] J. Li, D.J. Mooney, Designing hydrogels for controlled drug delivery, Nat. Rev. Mater. 1 (2016), 16071.

[24] L. Chengnan, Q. Pagneux, A. Voronova, A. Barras, A. Abderrahmani, V. Plaisance, V. Pawlowski, N. Hennuyer, B. Staels, L. Rosselle, N. Skandrani, M. Li, R. Boukherroub, S. Szunerits, Near-infrared light activatable hydrogels for metformin delivery, Nanoscale 11 (2019) 15810–15820.

[25] M. Gellert, M.N. Lipsett, D.R. Davies, Helix Formation by guanylic acid, Proc. Natl. Acad. Sci. U. S. A. 48 (1962) 2013–2018.

[26] Y.L. Wu, N.E. Horwitz, K.S. Chen, D.A. Gomez-Gualdron, N.S. Luu, L. Ma, T.C. Wang, M.C. Hersam, J.T. Hupp, O.K. Farha, R.Q. Snurr, M.R. Wasielewski, G-quadruplex organic frameworks, Nat. Chem. 9 (2017) 466–472.

[27] X.Q. Xie, Y. Zhang, M. Wang, Y. Liang, Y. Cui, J. Li, C.S. Liu, Programmable transient supramolecular chiral G-quadruplex hydrogels via a chemically fueled non-equilibrium self-assembly strategy, Angew Chem. Int. Ed. Engl. 61 (2021), e202114471.

[28] N. Thakur, B. Sharma, S. Bishnoi, S. Jain, D. Nayak, T.K. Sarma, Biocompatible Fe^{3+} and Ca^{2+} dual cross-linked G-quadruplex hydrogels as effective drug delivery system for pH-responsive sustained zero-order release of doxorubicin, ACS Appl. Bio Mater. 2 (2019) 3300–3311.

[29] A. Biswas, S. Malferrari, D.M. Kalaskar, A.K. Das, Arylboronate esters mediated self-healable and biocompatible dynamic G-quadruplex hydrogels as promising 3D-bioinks, Chem. Commun. 54 (2018) 1778–1781.

[30] V. Venkatesh, N.K. Mishra, I. Romero-Canelon, R.R. Vernooij, H. Shi, J.P.C. Coverdale, A. Habtemariam, S. Verma, P.J. Sadler, Supramolecular photoactivatable anticancer hydrogels, J. Am. Chem. Soc. 139 (2017) 5656–5659.

[31] Y. Jiang, N. Krishnan, J. Heo, R.H. Fang, L. Zhang, Nanoparticle-hydrogel superstructures for biomedical applications, J. Contr. Release 324 (2020) 505–521.

[32] J. Chen, C. Yu, Y. Zhao, Y. Niu, L. Zhang, Y. Yu, J. Wu, J. He, A novel non-invasive detection method for the FGFR3 gene mutation in maternal plasma for a fetal achondroplasia diagnosis based on signal amplification by hemin-MOFs/PtNPs, Biosens. Bioelectron. 91 (2017) 892–899.

[33] A. Sahu, I. Kwon, G. Tae, Improving cancer therapy through the nanomaterials-assisted alleviation of hypoxia, Biomaterials 228 (2020), 119578.

[34] H. Chen, W. He, Z. Guo, An H_2O_2-responsive nanocarrier for dual-release of platinum anticancer drugs and O_2: controlled release and enhanced cytotoxicity against cisplatin resistant cancer cells, Chem. Commun. 50 (2014) 9714–9717.

[35] P. Prasad, C.R. Gordijo, A.Z. Abbasi, A. Maeda, A. Ip, A.M. Rauth, R.S. DaCosta, X.Y. Wu, Multifunctional albumin-MnO_2 nanoparticles modulate solid tumor microenvironment by attenuating hypoxia, acidosis, vascular endothelial growth factor and enhance radiation response, ACS Nano 8 (2014) 3202–3212.

[36] Y. Zhang, F. Wang, C. Liu, Z. Wang, L. Kang, Y. Huang, K. Dong, J. Ren, X. Qu, Nanozyme decorated metal-organic frameworks for enhanced photodynamic therapy, ACS Nano 12 (2018) 651–661.

[37] C.-P. Liu, T.-H. Wu, C.-Y. Liu, K.-C. Chen, Y.-X. Chen, G.-S. Chen, S.-Y. Lin, Self-supplying O through the catalase-like activity of gold nanoclusters for photodynamic therapy against hypoxic cancer cells, Small 13 (2017), 1700278.

[38] X. Wang, Y. Hu, H. Wei, Nanozymes in bionanotechnology: from sensing to therapeutics and beyond, Inorg. Chem. Front. 3 (2016) 41–60.

[39] Z. Huang, Y. Wang, D. Yao, J. Wu, Y. Hu, A. Yuan, Nanoscale coordination polymers induce immunogenic cell death by amplifying radiation therapy mediated oxidative stress, Nat. Commun. 12 (2021) 145.

[40] L. Chen, L. Zhou, C. Wang, Y. Han, Y. Lu, J. Liu, X. Hu, T. Yao, Y. Lin, S. Liang, S. Shi, C. Dong, Tumor-targeted drug and CpG delivery system for phototherapy and docetaxel-enhanced immunotherapy with polarization toward M1-Type macrophages on triple negative breast cancers, Adv. Mater. 31 (2019), e1904997.

[41] L. Zhou, J. Chen, R. Li, L. Wei, H. Xiong, C. Wang, K. Chai, M. Chen, Z. Zhu, T. Yao, Y. Lin, C. Dong, S. Shi, Metal-polyphenol-network coated prussian blue nanoparticles for synergistic ferroptosis and apoptosis via triggered GPX4 inhibition and concurrent in situ bleomycin toxification, Small 17 (2021), e2103919.

[42] W. Zhao, X. Hu, W. Li, R. Li, J. Chen, L. Zhou, S. Qiang, W. Wu, S. Shi, C. Dong, M2-Like TAMs function reversal contributes to breast cancer eradication by combination dual immune checkpoint blockade and photothermal therapy, Small 17 (2021), e2007051.

[43] L. Feng, M.Y. Chen, R.H. Li, L.L. Zhou, C.H. Wang, P.T. Ye, X.C. Hu, J.X. Yang, Y.T. Sun, Z.N. Zhu, K. Fang, K.K. Chai, S. Shi, C.Y. Dong, Biodegradable oxygen-producing manganese-chelated metal organic frameworks for tumor-targeted synergistic chemo/photothermal/photodynamic therapy, Acta Biomater. 138 (2022) 463–477.

[44] B. Feng, Z.F. Niu, L. Zhou, Y.P. Li, H.J. Yu, Enhancing triple negative breast cancer immunotherapy by ICG-templated self-assembly of paclitaxel nanoparticles, Adv. Funct. Mater. 30 (2020).

[45] W.J. Shan, R.H. Chen, Q. Zhang, J. Zhao, B.B. Chen, X. Zhou, S.F. Ye, S.L. Bi, L.M. Nie, L. Ren, Improved stable indocyanine green (ICG)-mediated cancer optotheranostics with naturalized hepatitis B core particles, Adv. Mater. 30 (2018), 1707567.

[46] X.C. Hu, Y.L. Lu, L.L. Zhou, L. Chen, T.M. Yao, S.J. Liang, J.Y. Han, C.Y. Dong, S. Shi, Post-synthesis strategy to integrate porphyrinic metal-organic frameworks with CuS NPs for synergistic enhanced photo-therapy, J. Mater. Chem. B 8 (2020) 935–944.

[47] M.Y. Chen, J.X. Yang, L.L. Zhou, X.C. Hu, C.H. Wang, K.K. Chai, R.H. Li, L. Feng, Y.T. Sun, C.Y. Dong, S. Shi, Dual-responsive and ROS-augmented nanoplatform for chemo/photodynamic/chemodynamic combination therapy of triple negative breast cancer, Acs Appl Mater Inter 14 (2021) 57–68.

[48] B. Liu, X.Q. Gu, Q.N. Sun, S.J. Jiang, J. Sun, K. Liu, F. Wang, Y. Wei, Injectable in situ induced robust hydrogel for photothermal therapy and bone fracture repair, Adv. Funct. Mater. 31 (2021), 2010779.

[49] W. Yang, F. Zhang, H. Deng, L. Lin, S. Wang, F. Kang, G. Yu, J. Lau, R. Tian, M. Zhang, Z. Wang, L. He, Y. Ma, G. Niu, S. Hu, X. Chen, Smart nanovesicle-mediated immunogenic cell death through tumor microenvironment modulation for effective photodynamic immunotherapy, ACS Nano 14 (2020) 620–631.

[50] W. Li, J. Yang, L. Luo, M. Jiang, B. Qin, H. Yin, C. Zhu, X. Yuan, J. Zhang, Z. Luo, Y. Du, Q. Li, Y. Lou, Y. Qiu, J. You, Targeting photodynamic and photothermal therapy to the endoplasmic reticulum enhances immunogenic cancer cell death, Nat. Commun. 10 (2019) 3349.

[51] D.V. Krysko, A.D. Garg, A. Kaczmarek, O. Krysko, P. Agostinis, P. Vandenabeele, Immunogenic cell death and DAMPs in cancer therapy, Nat. Rev. Cancer 12 (2012) 860–875.

[52] X. Liu, B. Yan, Y. Li, X. Ma, W. Jiao, K. Shi, T. Zhang, S. Chen, Y. He, X.J. Liang, H. Fan, Graphene oxide-grafted magnetic nanorings mediated magnetothermodynamic therapy favoring reactive oxygen species-related immune response for enhanced antitumor efficacy, ACS Nano 14 (2020) 1936–1950.

[53] G. Kroemer, L. Galluzzi, O. Kepp, L. Zitvogel, Immunogenic cell death in cancer therapy, Annu. Rev. Immunol. 31 (2013) 51–72.

[54] S.N. Sethuraman, M.P. Singh, G. Patil, S. Li, S. Fiering, P.J. Hoopes, C. Guha, J. Malayer, A. Ranjan, Novel calreticulin-nanoparticle in combination with focused ultrasound induces immunogenic cell death in melanoma to enhance antitumor immunity, Theranostics 10 (2020) 3397–3412.

[55] F. Sun, Q. Zhu, T. Li, M. Saeed, Z. Xu, F. Zhong, R. Song, M. Huai, M. Zheng, C. Xie, L. Xu, H. Yu, Regulating glucose metabolism with prodrug nanoparticles for promoting photoimmunotherapy of pancreatic cancer, Adv. Sci. 8 (2021), 2002746.